CH$_3$NH$_3$PbI$_3$ perovskite / silicon tandem solar cells: characterization based optical simulations

Miha Filipič,[1,*] Philipp Löper,[2] Bjoern Niesen,[2] Stefaan De Wolf,[2] Janez Krč,[1] Christophe Ballif,[2] and Marko Topič[1]

[1] *University of Ljubljana, Faculty of Electrical Engineering, Tržaška 25, SI-1000 Ljubljana, Slovenia*
[2] *Ecole Polytechnique Fédérale de Lausanne (EPFL), Institute of Microengineering (IMT), Photovoltaics and Thin-Film Electronics Laboratory, Maladière 71, CH-2000 Neuchâtel, Switzerland*
*miha.filipic@fe.uni-lj.si

Abstract: In this study we analyze and discuss the optical properties of various tandem architectures: mechanically stacked (four-terminal) and monolithically integrated (two-terminal) tandem devices, consisting of a methyl ammonium lead triiodide (CH$_3$NH$_3$PbI$_3$) perovskite top solar cell and a crystalline silicon bottom solar cell. We provide layer thickness optimization guidelines and give estimates of the maximum tandem efficiencies based on state-of-the-art sub cells. We use experimental complex refractive index spectra for all involved materials as input data for an in-house developed optical simulator CROWM. Our characterization based simulations forecast that with optimized layer thicknesses the four-terminal configuration enables efficiencies over 30%, well above the current single-junction crystalline silicon cell record of 25.6%. Efficiencies over 30% can also be achieved with a two-terminal monolithic integration of the sub-cells, combined with proper selection of layer thicknesses.

OCIS codes: (350.6050) Solar energy; (160.6000) Semiconductor materials.

References and links

1. International Technology Roadmap for Photovoltaics," http://www.itrpv.net/Reports/Downloads/2014/.
2. W. Shockley and H. J. Queisser, "Detailed Balance Limit of Efficiency of p-n Junction Solar Cells," J. Appl. Phys. **32**(3), 510 (1961).
3. A. Richter, M. Hermle, and S. W. Glunz, "Reassessment of the Limiting Efficiency for Crystalline Silicon Solar Cells," IEEE J. Photovoltaics **3**(4), 1184–1191 (2013).
4. K. Masuko, M. Shigematsu, T. Hashiguchi, D. Fujishima, M. Kai, N. Yoshimura, T. Yamaguchi, Y. Ichihashi, T. Yamanishi, T. Takahama, M. Taguchi, E. Maruyama, S. Okamoto, T. Mishima, N. Matsubara, T. Yamanishi, T. Takahama, M. Taguchi, E. Maruyama, and S. Okamoto, "Achievement of More Than 25% Conversion Efficiency With Crystalline Silicon Heterojunction Solar Cell," IEEE J. Photovoltaics **4**(6), 1433–1435 (2014).
5. R. M. Swanson, "Approaching the 29% limit efficiency of silicon solar cells," Conf. Rec. Thirty-first IEEE Photovolt. Spec. Conf. 889–894 (2005).
6. S. P. Bremner, M. Y. Levy, and C. B. Honsberg, "Analysis of tandem solar cell efficiencies under AM1.5G spectrum using a rapid flux calculation method," Prog. Photovolt. Res. Appl. **16**(3), 225–233 (2008).
7. S. Kurtz and J. Geisz, "Multijunction solar cells for conversion of concentrated sunlight to electricity," Opt. Express **18**(S1), 73–78 (2010).
8. M. Imaizumi, M. Takahashi, and T. Takamoto, "JAXA's strategy for development of high-performance space photovoltaics," in *IEEE Photovoltaic Specialists Conference* (IEEE, 2010), pp. 128–131.
9. A. Shah, P. Torres, R. Tscharner, N. Wyrsch, and H. Keppner, "Photovoltaic Technology: The Case for Thin-Film Solar Cells," Science **285**(5428), 692–698 (1999).
10. D. Xiong and W. Chen, "Recent progress on tandem structured dye-sensitized solar cells," Front. Optoelectron. **5**(4), 371–389 (2012).
11. L. Dou, J. You, J. Yang, C.-C. Chen, Y. He, S. Murase, T. Moriarty, K. Emery, G. Li, and Y. Yang, "Tandem polymer solar cells featuring a spectrally matched low-bandgap polymer," Nat. Photonics **6**(3), 180–185 (2012).
12. X. Wang, G. I. Koleilat, J. Tang, H. Liu, I. J. Kramer, R. Debnath, L. Brzozowski, D. A. R. Barkhouse, L. Levina, S. Hoogland, and E. H. Sargent, "Tandem colloidal quantum dot solar cells employing a graded recombination layer," Nat. Photonics **5**(8), 480–484 (2011).

13. W.-S. Jeong, J.-W. Lee, S. Jung, J. H. Yun, and N.-G. Park, "Evaluation of external quantum efficiency of a 12.35% tandem solar cell comprising dye-sensitized and CIGS solar cells," Sol. Energy Mater. Sol. Cells **95**(12), 3419–3423 (2011).
14. G. D. Barber, P. G. Hoertz, S.-H. A. Lee, N. M. Abrams, J. Mikulca, T. E. Mallouk, P. Liska, S. M. Zakeeruddin, M. Grätzel, A. Ho-Baillie, and M. A. Green, "Utilization of Direct and Diffuse Sunlight in a Dye-Sensitized Solar Cell — Silicon Photovoltaic Hybrid Concentrator System," J. Phys. Chem. Lett. **2**(6), 581–585 (2011).
15. J. H. Seo, D.-H. Kim, S.-H. Kwon, M. Song, M.-S. Choi, S. Y. Ryu, H. W. Lee, Y. C. Park, J.-D. Kwon, K.-S. Nam, Y. Jeong, J.-W. Kang, and C. S. Kim, "High efficiency inorganic/organic hybrid tandem solar cells," Adv. Mater. **24**(33), 4523–4527 (2012).
16. C. D. Bailie, M. G. Christoforo, J. P. Mailoa, A. R. Bowring, E. L. Unger, W. H. Nguyen, J. Burschka, N. Pellet, J. Z. Lee, M. Grätzel, R. Noufi, T. Buonassisi, A. Salleo, and M. D. McGehee, "Semi-transparent perovskite solar cells for tandems with silicon and CIGS," Energy Environ. Sci., doi: 10.1039/C4EE03322A, (posted 23 December 2014, in press).
17. P. Löper, S.-J. Moon, S. M. de Nicolas, B. Niesen, M. Ledinsky, S. Nicolay, J. Bailat, J.-H. Yum, S. De Wolf, and C. Ballif, "Organic-inorganic halide perovskite/crystalline silicon four-terminal tandem solar cells," Phys. Chem. Chem. Phys. **17**(3), 1619–1629 (2014).
18. T. Todorov, T. Gershon, O. Gunawan, C. Sturdevant, and S. Guha, "Perovskite-kesterite monolithic tandem solar cells with high open-circuit voltage," Appl. Phys. Lett. **105**(17), 173902 (2014).
19. H. Zhou, Q. Chen, G. Li, S. Luo, T. B. Song, H.-S. Duan, Z. Hong, J. You, Y. Liu, and Y. Yang, "Photovoltaics. Interface engineering of highly efficient perovskite solar cells," Science **345**(6196), 542–546 (2014).
20. M. M. Lee, J. Teuscher, T. Miyasaka, T. N. Murakami, and H. J. Snaith, "Efficient hybrid solar cells based on meso-superstructured organometal halide perovskites," Science **338**(6107), 643–647 (2012).
21. S. De Wolf, J. Holovsky, S.-J. Moon, P. Löper, B. Niesen, M. Ledinsky, F.-J. Haug, J.-H. Yum, and C. Ballif, "Organometallic Halide Perovskites: Sharp Optical Absorption Edge and Its Relation to Photovoltaic Performance," J. Phys. Chem. Lett. **5**(6), 1035–1039 (2014).
22. J. H. Noh, S. H. Im, J. H. Heo, T. N. Mandal, and S. I. Seok, "Chemical Management for Colorful, Efficient, and Stable Inorganic-Organic Hybrid Nanostructured Solar Cells," Nano Lett. **13**(4), 1764–1769 (2013).
23. N. J. Jeon, H. G. Lee, Y. C. Kim, J. Seo, J. H. Noh, J. Lee, and S. I. Seok, "o-Methoxy substituents in spiro-OMeTAD for efficient inorganic-organic hybrid perovskite solar cells," J. Am. Chem. Soc. **136**(22), 7837–7840 (2014).
24. P. Löper, B. Niesen, S.-J. Moon, S. Martin de Nicolas, J. Holovsky, Z. Remes, M. Ledinsky, F.-J. Haug, J.-H. Yum, S. De Wolf, and C. Ballif, "Organic–Inorganic Halide Perovskites: Perspectives for Silicon-Based Tandem Solar Cells," IEEE J. Photovoltaics **4**(6), 1545–1551 (2014).
25. N. N. Lal, T. P. White, and K. R. Catchpole, "Optics and Light Trapping for Tandem Solar Cells on Silicon," IEEE J. Photovoltaics **4**(6), 1380–1386 (2014).
26. B. W. Schneider, N. N. Lal, S. Baker-Finch, and T. P. White, "Pyramidal surface textures for light trapping and antireflection in perovskite-on-silicon tandem solar cells," Opt. Express **22**(S6 Suppl 6), A1422–A1430 (2014).
27. C.-W. Chen, S.-Y. Hsiao, C.-Y. Chen, H.-W. Kang, Z.-Y. Huang, and H.-W. Lin, "Optical Properties of Organometal Halide Perovskite Thin Films and General Device Structure Design Rules for Perovskite Single and Tandem Solar Cells," J. Mater. Chem. A, doi: 10.1039/C4TA05237D, (posted 31 October 2014, in press).
28. P. Löper, B. B. Niesen, J. Werner, S.-J. Moon, M. Filipič, M. Topič, Y. Yum, S. De Wolf, and C. Ballif, "Complex refractive index of methyl ammonium lead halide determined from spectroscopic ellipsometry," J. Phys. Chem. Lett. **6**, 66–71 (2015).
29. H. J. Snaith, "Perovskites: The Emergence of a New Era for Low-Cost, High-Efficiency Solar Cells," J. Phys. Chem. Lett. **4**(21), 3623–3630 (2013).
30. Q. Chen, H. Zhou, Z. Hong, S. Luo, H.-S. Duan, H.-H. Wang, Y. Liu, G. Li, and Y. Yang, "Planar Heterojunction Perovskite Solar Cells via Vapor-Assisted Solution Process," J. Am. Chem. Soc. **136**(2), 622–625 (2014).
31. M. Liu, M. B. Johnston, and H. J. Snaith, "Efficient planar heterojunction perovskite solar cells by vapour deposition," Nature **501**(7467), 395–398 (2013).
32. D. Liu and T. L. Kelly, "Perovskite solar cells with a planar heterojunction structure prepared using room-temperature solution processing techniques," Nat. Photonics **8**(2), 133–138 (2013).
33. M. Taguchi, A. Yano, S. Tohoda, K. Matsuyama, Y. Nakamura, T. Nishiwaki, K. Fujita, and E. Maruyama, "24.7% Record efficiency HIT solar cell on thin silicon wafer," IEEE J. Photovoltaics **4**(1), 96–99 (2014).
34. Z. C. Holman, S. De Wolf, and C. Ballif, "Improving metal reflectors by suppressing surface plasmon polaritons: a priori calculation of the internal reflectance of a solar cell," Light Sci. Appl. **2**(10), e106 (2013).
35. Z. C. Holman, A. Descoeudres, S. De Wolf, and C. Ballif, "Record Infrared Internal Quantum Efficiency in Silicon Heterojunction Solar Cells With Dielectric/Metal Rear Reflectors," IEEE J. Photovoltaics **3**(4), 1243–1249 (2013).
36. B. Lipovšek, J. Krč, and M. Topič, "Optical model for thin-film photovoltaic devices with large surface textures at the front side," Inf. Midem – J. Microelectron. Electron. Components Mater. **41**, 264–271 (2011).
37. S. C. Baker-Finch and K. R. McIntosh, "Reflection of normally incident light from silicon solar cells with pyramidal texture," Prog. Photovolt. Res. Appl. **19**(4), 406–416 (2011).

38. J. Eisenlohr, J. Benick, M. Peters, B. Bläsi, J. C. Goldschmidt, and M. Hermle, "Hexagonal sphere gratings for enhanced light trapping in crystalline silicon solar cells," Opt. Express **22**(S1), A111–A119 (2014).
39. M. Bonnet-Eymard, M. Boccard, G. Bugnon, F. Sculati-Meillaud, M. Despeisse, and C. Ballif, "Optimized short-circuit current mismatch in multi-junction solar cells," Sol. Energy Mater. Sol. Cells **117**, 120–125 (2013).
40. J. H. Heo, S. H. Im, J. H. Noh, T. N. Mandal, C.-S. Lim, J. A. Chang, Y. H. Lee, H. Kim, A. Sarkar, M. K. Nazeeruddin, M. Grätzel, and S. Il Seok, "Efficient inorganic–organic hybrid heterojunction solar cells containing perovskite compound and polymeric hole conductors," Nat. Photonics **7**(6), 486–491 (2013).
41. M. J. Dodge, "Refractive properties of magnesium fluoride," Appl. Opt. **23**(12), 1980 (1984).
42. Z. C. Holman, M. Filipič, A. Descoeudres, S. De Wolf, F. Smole, M. Topič, and C. Ballif, "Infrared light management in high-efficiency silicon heterojunction and rear-passivated solar cells," J. Appl. Phys. **113**(1), 013107 (2013).
43. M. Topič, A. Čampa, M. Filipič, M. Berginc, U. O. Krašovec, F. Smole, and U. Opara Krašovec, "Optical and electrical modelling and characterization of dye-sensitized solar cells," Curr. Appl. Phys. **10**(3), S425–S430 (2010).
44. J. Springer, A. Poruba, and M. Vanecek, "Improved three-dimensional optical model for thin-film silicon solar cells," J. Appl. Phys. **96**(9), 5329 (2004).
45. M. Green, "Self-consistent optical parameters of intrinsic silicon at 300K including temperature coefficients," Sol. Energy Mater. Sol. Cells **92**(11), 1305–1310 (2008).
46. E. D. Palik, *Handbook of Optical Constants of Solids* (Academic Press, 1997).
47. A. J. Moulé, H. J. Snaith, M. Kaiser, H. Klesper, D. M. Huang, M. Grätzel, and K. Meerholz, "Optical description of solid-state dye-sensitized solar cells. I. Measurement of layer optical properties," J. Appl. Phys. **106**(7), 073111 (2009).
48. Z. C. Holman, A. Descoeudres, L. Barraud, F. Z. Fernandez, J. P. Seif, S. De Wolf, C. Ballif, and S. De Wolf, "Current Losses at the Front of Silicon Heterojunction Solar Cells," IEEE J. Photovoltaics **2**(1), 7–15 (2012).
49. C. Momblona, O. Malinkiewicz, C. Roldán-Carmona, A. Soriano, L. Gil-Escrig, E. Bandiello, M. Scheepers, E. Edri, and H. J. Bolink, "Efficient methylammonium lead iodide perovskite solar cells with active layers from 300 to 900 nm," APL Mater. **2**(8), 081504 (2014).

1. Introduction

Crystalline silicon (c-Si) solar cells have been dominating the photovoltaics market for several decades, with a current market share of 90% [1]. Even though the bandgap of c-Si is nearly ideal according to the Shockley-Queisser limit [2], Auger recombination restricts the conversion efficiency of silicon-based cells to 29.4% [3]. The current world record efficiency for c-Si solar cells of 25.6% was obtained with amorphous silicon (a-Si) / crystalline silicon heterojunction technology [4], which is already close to 26%, a value considered a "practical limit" of c-Si single-junction solar cells [5]. Despite this, for photovoltaics to become fully competitive with fossil and nuclear energy sources, even higher efficiencies at low cost may be required. One approach to move beyond the fundamental limit of c-Si is to use solar cells featuring multiple junctions, combining absorber materials that harvest different parts of the solar spectrum. This reduces thermalization and transmission losses. In a two-junction (tandem) configuration the theoretical limiting conversion efficiency under standard test conditions is 46.1% (with bandgaps of 1.73 and 0.94eV) and 45.7% (with bandgaps of 1.60 and 0.94eV) for four-terminal and two-terminal device, respectively [6].

The tandem concept has already been successfully implemented for high-efficiency concentrator cells [7], limited to regions with strong direct illumination, and to space applications [8]. For low-cost terrestrial photovoltaics, tandem solar cells have also been realized with various technologies, examples of which include amorphous and microcrystalline silicon solar cells [9], dye-sensitized solar cells (DSSC) [10], organic solar cells [11], quantum dot solar cells [12] and hybrid combinations like the DSSC / Cu(In,Ga)Se$_2$ solar cells [13], DSSC / silicon solar cells [14] or organic solar cells / silicon solar cells [15]. None of these tandem devices could yet surpass the single-junction c-Si efficiency due to the defective nature of the absorber materials. As a consequence, high-efficiency tandem solar cell fabrication at low cost has been elusive so far. This situation may change rapidly with the recent emergence of organic-inorganic perovskites as photovoltaic absorbers. First experimental examples of perovskite-based tandems can already be found in the literature [16–18].

Single-junction CH₃NH₃PbI₃ perovskite solar cells have made remarkable progress in recent years with reported efficiencies of more than 19% [19]. CH₃NH₃PbI₃ has a high absorption coefficient [20] and sharp absorption edge [21]. It also has a relatively large bandgap of 1.57 eV, with little sub-bandgap absorption [21], making it an appealing candidate for low-cost high-efficiency monolithic tandem solar cells. If we limit ourselves to c-Si bottom cells (bandgap of 1.12 eV), the ideal bandgap of the top cell is 1.75 eV [9]. By chemically tuning the composition of CH₃NH₃PbI₃, for example by partially substituting the iodine atoms with different halogens such as bromine, the perovskite bandgap can be increased to the ideal value [22]. The goal of this paper is to identify the most promising experimentally feasible devices. For this reason we restrict ourselves to CH₃NH₃PbI₃ as it is the state-of-the-art material that demonstrates high conversion efficiencies [19,23] and has a bandgap that is sufficiently close to the optimum to still allow for high efficiencies of tandem structures in combination with c-Si [24].

Optical simulation studies of perovskite / c-Si tandems based on *assumed* refractive indices and absorption coefficients for the CH₃NH₃PbI₃ perovskite can already be found in the literature [24–26]. Recently, the measured CH₃NH₃PbI₃ refractive index has been used for single-junction perovskite and tandem perovskite / Cu(In,Ga)Se₂ solar cell simulation [27].

In this article, we study the optical properties of the entire tandem structure consisting of a top CH₃NH₃PbI₃ perovskite solar cell and a bottom c-Si solar cell. Using optical simulations, we provide guidelines for layer thickness optimization, and we estimate the efficiency potential for several tandem device architectures, including mechanically stacked four-terminal and monolithically integrated two-terminal tandem cells. For all these architectures, we consider flat as well as textured c-Si bottom cells. We use experimentally determined complex refractive indices of all layers, including CH₃NH₃PbI₃ [28] and Spiro-OMeTAD, as simulation input parameters.
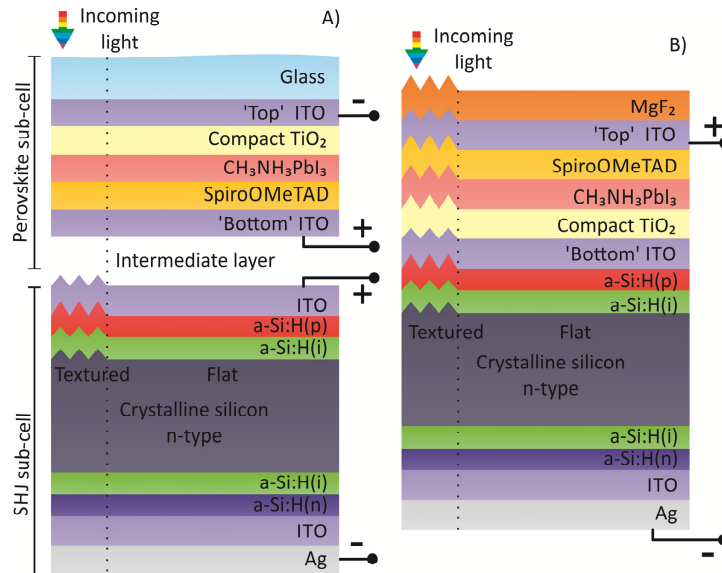

Fig. 1. Schematic representation of the simulated architectures: A) Four-terminal device, where individual CH₃NH₃PbI₃ perovskite and silicon cells are optically stacked. B) Two-terminal device with CH₃NH₃PbI₃ perovskite and silicon cells connected in series. On the left side textured wafers (front surface) and layers deposited on top by conformal growth are shown.

2. Experimental

The optical functions of Spiro-OMeTAD were determined by fitting an optical model to variable angle spectroscopic ellipsometry (VASE) data and reflectance and transmittance

spectra. To enhance the accuracy of the fit, a multi-sample analysis was performed using co-prepared films on c-Si and glass substrates.

Spiro-OMeTAD (2,2′,7,7′-tetrakis(*N*,*N*-di-*p*-methoxyphenylamine)-9,9-spirobifluorene) was purchased from Merck KGaA. 72.3 mg spiro-OMeTAD, 28.8 µl 4-tert-butylpyridine, 17.5 µl of a stock solution of 520 mg ml^{-1} lithium bis(trifluoromethylsulphonyl)imide in acetonitrile, and 21.9 µl of a stock solution of 400 mg ml^{-1} tris(2-(1H-pyrazol-1-yl)-4-tert-butylpyridine)-cobalt(III)Tris(bis(trifluoromethylsulfonyl)imide)) in acetonitrile were dissolved in 1 ml chlorobenzene and spin coated on 500 µm thick Schott AF32 glass and 280 µm thick double-side polished n-type 1 Ωcm (100) c-Si wafers at 4000 rpm for 30 s in a nitrogen atmosphere.

Reflectance and transmittance measurements were carried out using a Perkin Elmer Lambda 950 spectrophotometer between 320 nm and 2000 nm with a spectral resolution of 10 nm. Ellipsometry measurements were done in reflection mode using a Horiba Jobin Yvon UVISEL iHR320 polarization modulation ellipsometer under incident angles of 50°, 60° and 70° with a spectral resolution of 10 meV similarly as in [24]. The dielectric function is identified indirectly by fitting the data with a suitable model. The thicknesses of all films were measured with a KLA Tencor P16 + profilometer and held constant in the fit.

We model the complex dielectric function $\varepsilon(\omega)$ with four Lorentzian oscillators and a Cauchy contribution. The Lorentzian oscillators are described by a center frequency ω_t, a damping factor Γ_0, and the parameters ε_∞ and ε_s, describing the response of the oscillator at $\omega = 0$ and $\omega = \infty$, respectively.

$$\varepsilon = \varepsilon_\infty + \sum_{i=1}^{4} \frac{\left(\varepsilon_{s,i} - \varepsilon_\infty\right)\omega_{t,i}^2}{\omega_{t,i}^2 - \omega^2 + i\Gamma_{0,i}}. \tag{1}$$

The Cauchy contribution adds a term

$$n = n_\infty + \frac{B \times 10^4}{\lambda^2} + \frac{C \times 10^9}{\lambda^4} \tag{2}$$

to the real part of the dielectric function, with the three real parameters n_∞, B, and C.

All data, i.e. the ellipsometric measurement of spiro-OMeTAD on c-Si, as well as the reflectance and transmittance measurements of Spiro-OMeTAD on c-Si and glass were fitted (least squares) simultaneously in a bound model. The layer thicknesses were fixed to the values measured with the profilometer. A surface roughness was not accounted for. The parameters giving the best fit to the data are summarized in Table 2. The complex refractive index, $n-ik$ was calculated from the dielectric function, $\varepsilon = \varepsilon_1 - i\varepsilon_2$, with $\varepsilon_1 = n^2 - k^2$ and $\varepsilon_2 = 2nk$ and is shown in Fig. 2(a).

3. Model description

In this study we exclusively analyze perovskite cells in a planar thin-film configuration without mesoporous scaffold (A discussion of the different perovskite architectures has recently been published by Snaith [29]). Perovskite solar cells can be prepared with a variety of electron and hole transporting materials, either by vapor-deposition or solution processing [30–32]. We choose a structure based on a highly efficient $CH_3NH_3PbI_3$ perovskite cell [23], replacing the opaque metal back contact with transparent indium tin oxide (ITO) to enable transmission of infrared light to the bottom cell. To prevent sputter damage a thin metal oxide buffer, such as MoO_x layer, could be evaporated before the ITO deposition [17]. MoO_x has very similar refractive index to that of the ITO and only a very thin layer (~10 nm) is required to prevent sputter damage. Therefore its influence on the optical behavior of the tandem cell is minor and is not included in the model for simplicity. Our results can be applied to a broad

range of material combinations, provided that their optical properties are similar to the materials we use.

For the c-Si bottom cell, we employ amorphous silicon / crystalline silicon heterojunction (SHJ) cells, which use c-Si wafers as photoactive absorbers [4] and a-Si thin-films for junction formation and surface passivation. In a single-junction design, such cells exhibit high open-circuit voltages (V_{oc}) of up to 750 mV [33] thanks to high c-Si bulk lifetimes and excellent surface passivation. These cells are particularly well-suited for bottom cell applications from an electrical *and* optical perspective: Their high voltages are maintained at reduced illumination levels, and with proper light management [34] these cells exhibit excellent external quantum efficiency (EQE) response in the long-wavelength region [35]. Our results are also valid for other types of c-Si solar cells, such as diffused junction cells, as the a-Si layers and diffused regions influence the optical properties only marginally.

In our simulations of perovskite / SHJ tandem cells, we use experimentally extracted complex refractive indices of all involved layers. These spectra were taken from the literature for well described materials (references in Table 1), but for the $CH_3NH_3PbI_3$ perovskite [28] and Spiro-OMeTAD, we used our own data, determined from spectroscopic ellipsometry measurements. To simulate the optical properties of the tandem devices we used the optical simulator CROWM, which combines wave optics (transfer matrix method) for thin films and geometrical optics (ray-tracing) for textured surfaces, and was developed at the University of Ljubljana [36]. For illumination we use AM1.5G solar spectrum (IEC 60904).

3.1 Four-terminal model description

In the four-terminal tandem device, the top $CH_3NH_3PbI_3$ perovskite cell and the bottom SHJ cell are electrically independent. However, the cells are optically coupled, such that the light that is transmitted through the top cell reaches the bottom cell. For the model, the planar $CH_3NH_3PbI_3$ perovskite cell structure shown in Fig. 1(a) (top cell) is assumed, consisting here of a 2 mm thick glass superstrate followed by five thin-film layers (i.e. 'top' ITO, compact TiO_2, $CH_3NH_3PbI_3$, Spiro-OMeTAD and 'bottom' ITO). On top of the glass superstrate a thin MgF_2 layer can be added as an anti-reflective coating. We omit light scattering and model the layers with planar interfaces, which allows us to focus on interference effects.

The optical structure of the SHJ cell model shown in Fig. 1(a) (bottom cell) consists of a ITO (70 nm), p-type a-Si (10 nm), intrinsic a-Si (5 nm), c-Si absorber, intrinsic a-Si (5 nm), n-type a-Si (10 nm), ITO (150 nm), and a silver back reflector (300 nm). SHJ cells usually feature textured c-Si surfaces, consisting of randomly distributed pyramids prepared by alkaline-etching, with a characteristic angle of 54.7° (left side of Fig. 1(a)). These textured surfaces reduce the reflection and increase the optical path length in the cell [37]. Increased optical path length due to light trapping is a necessity for achieving high long-wavelength EQE response and consequently high efficiency SHJ and tandem cells. However, simulating light trapping effects is computationally intensive and not suitable for our multi-dimensional optimization task. To introduce the increased optical path length in our SHJ cell model we take a cell with flat surface and increase the optical thickness of the absorber material – we use a 3.5 mm thick c-Si layer. This thickness results in a similar long-wavelength response as an experimentally measured textured state-of-the-art SHJ cell (symbols in Fig. 3) [35]. With this approach our model has a much lower computation time but the results are comparable to the computationally demanding ray tracing routines. Our flat SHJ cell model therefore features a planar front surface, but still exhibits excellent light trapping properties, without the anti-reflection effect of the front side texture. In practice, planar front surface cells with ~100 μm thick absorbers and enhanced light path length, can be realized with structured rear surfaces, for example by using hexagonal sphere gratings [38]. For anti-reflection properties due to a texture, see the section on surface texture effects.

Between top and bottom cell in the four-terminal tandem, a thick non-absorbing intermediate light-coupling layer is assumed, for which the ideal wavelength independent

refractive index is to be determined. Since room for electrical contacts has to be available in the four-terminal device between the top and bottom cells, we assume that the intermediate layer is sufficiently thick to be incoherent and set its thickness to 2 mm. The glass superstrate is also modeled as an incoherent layer, implying that it does not cause interference effects.

Omitting ray tracing during optimization results in a computationally fast model, which enables us to optimize the structure in a 6-dimensional parameter space consisting of the combination of five layer thicknesses of the $CH_3NH_3PbI_3$ perovskite cell (excluding the glass layer) and the refractive index of the intermediate layer (assuming a non-absorbing layer, $k = 0$). We determine the values of these parameters that result in the highest combined efficiency of the $CH_3NH_3PbI_3$ perovskite and SHJ cells. To achieve this, we use the CROWM simulator to calculate the short-circuit current densities under the assumption that all photo-generated carriers are successfully collected (equivalent J_{sc}). We then apply this simulated J_{sc} value to the one-diode model of the single junction $CH_3NH_3PbI_3$ perovskite and SHJ cells from which we estimate the efficiency. The objective function for optimization maximizes the sum of efficiencies of the $CH_3NH_3PbI_3$ perovskite cell, η_{Per}, and the SHJ cell, η_{SHJ},

$$f_{4T} = \eta_{Per} + \eta_{SHJ}. \tag{3}$$

To obtain the one-diode model parameters we use a curve fitting routine to fit the current density-voltage characteristic (J-V) of the one-diode model with J-V curves reported in the literature. Although higher efficiencies are reported in literature, we choose a 16.7% efficient perovskite cell, since care was taken to minimize the error due to the hysteresis effect during the J-V measurement [23]. For the bottom cell we choose the record both-sides-contacted SHJ cell, which yields 24.7% certified efficiency [33]. The record SHJ cell of 25.6% is not chosen because it has all contacts on the back side of the cell [4], and is therefore not suitable for implementation of the two-terminal device.

Using one-diode parameters of the single-junction cells and using them in tandem optimization has some drawbacks. For instance, the areas of the cells are different (SHJ cell with 100 cm^2 vs. perovskite cell with <1 cm^2), making it difficult to directly compare the cell parameters. Moreover, structural changes required for tandem implementation such as absence of rear metal layers (four-terminal perovskite cell) and front metal grids (two-terminal SHJ cell) might influence the J_{sc} and series resistance, introducing some level of uncertainty to the parameters. To evaluate these effects a detailed characterization of single-junction devices or electrical modeling would be required. Nevertheless, using single-junction cell parameters as a basis for optimization and efficiency estimation still gives more realistic results than only the optimization of J_{sc} values.

3.2 Two-terminal model description

In the two-terminal tandem device the cells are optically stacked and electrically connected in series. The structure schematic is shown in Fig. 1(b). As the cells are monolithically integrated, the SHJ cell serves as the substrate for the perovskite cell deposition (instead of the commonly used glass). We chose a structure where the perovskite absorber is prepared on top of a compact TiO_2 layer, as most perovskite cells are prepared in this manner [30,31]. The perovskite preparation on TiO_2 dictates the polarity of the tandem, as in this case, hole collection occurs at the sun-exposed side. Therefore, compared to the four-terminal device, the polarity of the $CH_3NH_3PbI_3$ perovskite sub-cell has to be reversed. On top of the tandem structure an MgF_2 layer is added as an anti-reflective coating. For the two-terminal tandem, the $CH_3NH_3PbI_3$ perovskite cell is again modeled as a stack of five flat thin-film layers (in reversed order, compared to the four-terminal device, however). The SHJ cell model used in the optimization is the same as for the four-terminal tandem.

As the cells are connected in series in the monolithic tandem, the cell with the lower current limits the tandem cell power output and best efficiencies are achieved when the current at the maximum power point (MPP) of the perovskite cell J_{MPP}^{Per} is equal (matched) to

that of the SHJ cell J_{MPP}^{SHJ}. Note that this leads to a current mismatch at short-circuit conditions [39]. We take this constraint into account in the objective function during optimization:

$$f_{2T} = \eta_{Per} + \eta_{SHJ} - \left| J_{MPP}^{Per} - J_{MPP}^{SHJ} \right|. \tag{4}$$

Units of η are in % and units of J_{MPP} are in mA/cm^2 making their numeric values equal in magnitude. The objective function in Eq. (4) maximizes the sum of both efficiencies, while keeping their difference in current densities at MPP low. The efficiencies and current densities at MPP are obtained with the one-diode model and the optically simulated J_{sc} values as in the four-terminal case. During the 6-dimensional parameter optimization we searched for the combination of five CH$_3$NH$_3$PbI$_3$ perovskite cell layer thicknesses and SHJ ITO layer thickness that results in maximized objective function.

3.3 Surface texture effects

As mentioned previously, SHJ cells usually feature random pyramid textures. Inverted pyramids, employed in simulations by other authors [26], are interesting from an academic point of view, but due to cost reasons only random pyramid textures are relevant to the industry. After the flat layer thickness optimization, we run ray tracing simulations with a textured front surface of the SHJ cell, taking into account all possible reflections from the pyramids, to evaluate the anti-reflection effect of the texture on the tandem structure. The simulated texture consists of a periodic array of 5-µm-high upright pyramids with a characteristic angle of 54.7°. Since the front surface texture not only reduces reflection, but also increases the optical path length, the optical thickness of the absorber with a textured front surface has to be adjusted to 1.5 mm to yield a good agreement with the long-wavelength response of the measured SHJ cell [35]. Note that the optical absorber thickness is still larger than the usual ~100 µm thick SHJ cell absorber. The reason for this is that the back surface of the SHJ cell is flat in all cases considered here, and a thicker absorber is required to compensate for light trapping effects of the back texture.

For the two-terminal tandem, the perovskite cell is deposited on top of the textured SHJ surface and for a conformal thin-film layer stack on an ideal pyramid the light enters the perovskite cell at an incident angle of 54.7° (see left side of Fig. 1(b)). When simulating textured surfaces with ray tracing, we use perovskite cell layer thicknesses that were optimized at an oblique incidence of 54.7°. Note that optimization is carried out on flat thin-films and therefore the optimum is determined with respect to the incident ray only (rays reflected from pyramid faces are not included due to the low reflection of the optimized stack).

3.4 Optimization procedure

In both two- and four-terminal tandem devices the optimum is found by starting the optimization routines that converge to the local maximum from many randomly selected starting points (layer thickness combinations). When searching for the optimum we can constrain the search range of layer thicknesses. First we constrain the thicknesses to experimentally feasible ranges around typical values of our experimental devices, given in Table 1. For ITO layers, where a low sheet resistance is needed for lateral conduction (i.e. 'top' and 'bottom' ITO of the four-terminal perovskite cell and the 'top' ITO of the two-terminal tandem cell), the lower bound was chosen to be 60 nm. However, perovskite cells can be realized with alternative layer sequences and thickness constraints as the ones used here. For example, the compact TiO$_2$ or the Spiro-OMeTAD can be exchanged by other materials [32,40]. Therefore, we use in the second case more relaxed constraints, limiting each layer thickness to the range of 0 to 1000 nm. The layer thickness of 0 nm means the optical absence of that layer, which gives us an indication of which layers are most problematic and should be avoided when developing novel tandem architectures.

Layer	Thickness constraints (nm)	Source of *n* and *k*
MgF_2	0-200	[41]
'Top' ITO	60-150	[42]
Spiro-OMeTAD	100-300	This study
$CH_3NH_3PbI_3$	200-350	[28]
Compact TiO_2	10-80	[43]
'Bottom' ITO	60-150 (4T) or 20-150 (2T)	[42]
a-Si layers	Not varied	[44]
c-Si	Not varied	[45]
Ag	Not varied	[46]

4. Results and discussion

4.1 Spiro-OMeTAD refractive index

The best fit to the experimental spectra is shown in Fig. 2(b) and 2(b). The calculated spectra (lines) agree very well with the experimental spectra (symbols) over the entire measured spectral range. The fit parameters are listed in Table 2, and the resulting complex refractive index is plotted in Fig. 2(a). Our result is well comparable to that reported by Moule et al. [47] which was obtained with slightly differently doped spiro-OMeTAD films. The agreement between the experimental spectra on multiple samples increases the reliability of our result.

Table 2. Parameters of the dielectric function model, giving the best fit to the data.

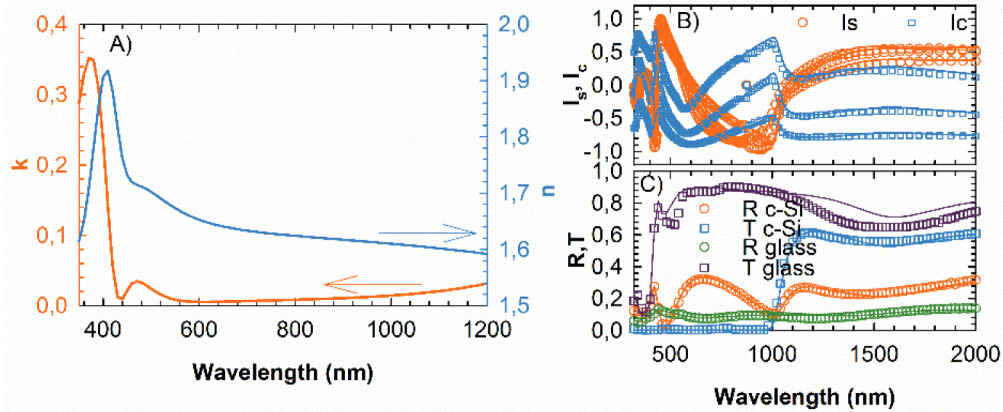|									
n_∞	1.57	$\varepsilon_{s,1}$	0.69	$\varepsilon_{s,2}$	2.06	$\varepsilon_{s,3}$	1.15	$\varepsilon_{s,4}$	0.48
B	−1.55	$\omega_{t,1}$	2.94	$\omega_{t,2}$	3.09	$\omega_{t,3}$	0.78	$\omega_{t,4}$	2.81
C	3.44	Γ_1	0.52	Γ_2	1.11	Γ_3	0.26	Γ_4	1.40
ε_∞	1.00								

Fig. 2. A) Real part *n* and imaginary part *k* of the refractive index of Spiro-OMeTAD. B) VASE experimental spectra (symbols) and calculated spectra (lines) of Spiro-MeOTAD on c-Si substrate. C) Reflection and transmission experimental spectra (symbols) and calculated spectra (lines) on a glass and c-Si substrates.

4.2 Extracted one-diode parameters

Table 3 lists the one-diode model parameters obtained by fitting the model to the reported *J-V* curves under illumination [23,33], where J_L is the photo-generated current density, J_0 the saturation current density, *n* the ideality factor, R_S the series resistance and R_{SH} the shunt resistance. During optimization, the value of J_L is replaced with simulated J_{sc} value.

Table 3. One-diode parameters of single junction cells, extracted by fiting from literature data.

Cell	J_L (mA/cm^2)	J_0 (mA/cm^2)	n	R_S ($\Omega \times$ cm^2)	R_{SH} ($\Omega \times$ cm^2)
Perovskite	21.2	4.93×10^{-7}	2.20	0.48	8.90×10^3
SHJ	39.4	8.21×10^{-10}	1.17	0.07	8.84×10^5

4.3 Four-terminal optimization

Table 4 shows the optimal values of the varied parameters for the flat and textured four-terminal tandem device. In addition, it also gives the most significant equivalent J_{sc} values for the constrained case (thickness limits in Table 1) and the unconstrained case (thickness limit from 0 to 1000 nm). For the constrained cases (flat and textured), most of the thicknesses are close to the assumed boundaries, indicating that the true optimum might actually lie outside these limits. This is indeed confirmed by the unconstrained simulations. Notably, the thicknesses of layers in which parasitic absorption dominates over possible anti-reflection properties converge to 0 nm in the optimum case, equivalent to the optical absence of the involved layer. Despite this, the unconstrained optimum represents the J_{sc} limit for the given device structure and may give guidance to future device design.

Table 4. Optimal parameter values of the four-terminal tandem device with equivalent J_{sc} values of selected layers without the MgF$_2$ anti-reflection layer.

	Flat		Textured	
Varied parameters	Constrained	Unconstrained	Constrained	Unconstrained
'Top' ITO thickness (nm)	61	67	61	67
Compact TiO$_2$ thick. (nm)	10	14	10	14
CH$_3$NH$_3$PbI$_3$ thickness (nm)	350	1000	350	1000
Spiro-OMeTAD thick. (nm)	100	0	100	0
'Bottom' ITO thick. (nm)	60	95	60	95
Intermediate layer n ()	1.8	1.6	1.8	1.6
Equivalent J_{sc} (mA/cm^2)				
Perovskite absorber	20.1	23.3	19.9	23.3
SHJ absorber	17.9	16.0	19.6	17.7
Reflection	6.7	5.7	4.6	2.8
Spiro-OMeTAD	0.5	0.0	0.7	0.0
'Top' ITO	0.4	0.5	0.5	0.6
'Bottom' ITO	0.2	0.3	0.3	0.8

Due to the higher bandgap of the CH$_3$NH$_3$PbI$_3$ perovskite compared to the c-Si absorber of the SHJ cell, thermalization losses of high energy photons are lower if they are absorbed in the perovskite cell. Therefore it is advantageous to absorb as much high energy photons as possible in the top cell. Since CH$_3$NH$_3$PbI$_3$ absorbs up to wavelengths of 800 nm, highest efficiencies are achieved when most of the light at wavelengths up to 800 nm is absorbed in the perovskite cell while simultaneously all light above 800 nm is transmitted to the SHJ cell. For the unconstrained cases, this leads to a thick CH$_3$NH$_3$PbI$_3$ layer, which absorbs all the light below 800 nm in the perovskite cell. The reflection of the flat tandem device and absorption in each individual layer are displayed in Fig. 3. In the constrained case, an equivalent of 3.1 mA/cm^2 is absorbed in the c-Si wafer in the wavelength range between 500 and 800 nm, which ideally should have been absorbed in the CH$_3$NH$_3$PbI$_3$ layer.

Despite the fact that in the four-terminal tandem device Spiro-OMeTAD is positioned at the bottom of the perovskite cell, it turns out to be the layer with highest parasitic absorption (at optimized thickness) in the constrained case, as seen in Table 4. This is a consequence of the fact that Spiro-OMeTAD considerably absorbs light in the visible and also the infrared due to the presence of dopants in the Spiro-OMeTAD layer, required for high-efficiency devices, resulting in reduced transmission of light to the SHJ cell. In the unconstrained case this layer is absent, indicating that the absorption dominates over possible benefits from interference effects. In the long-wavelength range, the bottom ITO also contributes to

parasitic absorption, caused by free carrier absorption, but its thickness is increased in the unconstrained case, suggesting that beneficial interference effects outweigh the absorption losses. These results confirm the necessity to develop highly NIR-transparent charge transport layers. In the UV range, parasitic absorption losses occur in the glass, the compact TiO_2 and the 'top' ITO. The glass thickness was fixed at 2 mm and there are only minimal changes in its absorption between the constrained and the unconstrained case. Small differences are also observed in the 'top' ITO thickness, where anti-reflection properties outweigh the parasitic absorption. Short-wavelength light, where a-Si layers parasitically absorb in single-junction SHJ solar cells [48], is actively absorbed in the top cell and does not reach the bottom cell. Therefore, a-Si layers do not contribute to parasitic absorption in the tandem. The optimal constant refractive index of the intermediate layer for the unconstrained case is 1.6, which is near the constrained value of 1.8.
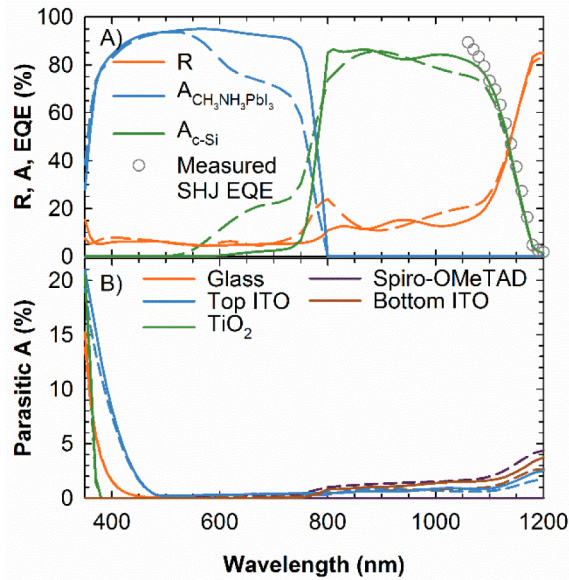

Fig. 3. Reflection and absorption plots for the flat four-terminal tandem configuration without the MgF_2 anti-reflection layer. A) Reflection of the tandem stack, and absorption in the active layers. B) Parasitic absorption of layers in the $CH_3NH_3PbI_3$ perovskite cell. Dashed lines represent the optimal results of the constrained case, while full lines show optimum results when the thicknesses were unconstrained. Grey circle symbols in the top plot represent the measured EQE of a SHJ cell [35].

For four-terminal tandems with textured SHJ bottom cells we assume the same optimal perovskite layer thicknesses as with a flat surface. The main difference when introducing a textured front SHJ surface is the reduced reflection of light from the bottom cell above wavelengths of 800 nm. In the unconstrained case, most of the light below 800 nm is absorbed in the perovskite cell and a surface texture of the bottom cell does not have any effect on the perovskite cell current. In the constrained case less light up to wavelengths of 800 nm is reflected back from the textured than from a flat SHJ bottom cell, which reduces the perovskite cell current by 0.2 mA/cm^2. Therefore we conclude that the bottom cell surface texture has only a minor effect on the perovskite cell, supporting our initial assumption of similar optimal perovskite cell thicknesses for either a flat or textured SHJ cell. Even so, having a texture is beneficial for the bottom cell, as less light above 800 nm is reflected and its J_{sc} is consequently increased relative to a flat bottom cell. In both the constrained and unconstrained case, the surface texture increases the bottom cell current by 1.7 mA/cm^2. Another effect of the texture is the increased parasitic absorption in the Spiro-OMeTAD and

ITO layers at wavelengths where the c-Si absorber is weakly absorbing (>1100 nm). This is due to the increased optical path length of light reflected from the SHJ back reflector which then travels back through the perovskite cell, where it is parasitically absorbed in Spiro-OMeTAD and ITO layers.

Finally, when a 114 nm thick MgF_2 layer that minimizes the reflection, is deposited on the top side of the perovskite cell as an anti-reflection coating (not shown in Fig. 1(a)), the perovskite cell J_{sc} is increased by 0.5 mA/cm^2 and 0.6 mA/cm^2 for the constrained and the unconstrained case, respectively, and the SHJ cell J_{sc} by 0.4 mA/cm^2 in both cases. Since the two-terminal tandem device studied here also features an anti-reflection MgF_2 layer, we take these values into account when estimating efficiencies of the tandem cells to allow for a better comparability between the various device architectures.

4.4 Two-terminal optimization

For the flat two-terminal device, the optimal layer thicknesses for the constrained and unconstrained cases together with most significant equivalent J_{sc} values are displayed in Table 5. The flat unconstrained case again shows that the layers in which parasitic absorption dominates over anti-reflection properties converge to a thickness of 0 nm. Since the two sub-cells need to be current matched for best performance, the $CH_3NH_3PbI_3$ thickness does not go to as high values as in the four-terminal device. Figure 4 shows the reflection of the flat tandem device and the absorption for the individual layers. In the optimal unconstrained two-terminal tandem device the $CH_3NH_3PbI_3$ perovskite cell acts as an anti-reflection coating for the SHJ cell, which leads to a reflectance below 5% in the wavelength range of 500 to 1000 nm.

Table 5. Optimal layer thicknesses for constrained and unconstrained optimization of the two-terminal device with flat or textured bottom cell surface.

	Flat		Textured	
Varied parameters (nm)	Constrained	Unconstrained	Constrained	Unconstrained
MgF_2 thickness	105	109	119	142
'Top' ITO thickness	127	52	123	58
Spiro-OMeTAD thickness	155	0	156	0
$CH_3NH_3PbI_3$ thickness	350	437	350	421
Compact TiO_2 thickness	79	72	10	83
'Bottom' ITO thickness	37	0	68	0
Equivalent J_{sc} (mA/cm^2)				
Perovskite absorber	18.4	21.7	19.2	22.0
SHJ absorber	18.0	21.2	19.3	21.2
Reflection	6.2	2.7	3.0	2.2
Spiro-OMeTAD	2.4	0.0	3.0	0.0
'Top' ITO	1.0	0.4	1.2	0.6
'Bottom' ITO	0.1	0.0	0.2	0.0

Due to the inverted polarity of the perovskite cell in the two-terminal tandem, the $CH_3NH_3PbI_3$ absorber is illuminated through the Spiro-OMeTAD layer, which introduces additional parasitic absorption in the short-wavelength range not present in the four-terminal device. In the constrained case, Spiro-OMeTAD absorption is as high as 50% in the UV, which surpasses UV parasitic absorption in the four-terminal configuration. This parasitic absorption greatly reduces the performance of the constrained two-terminal device indicating that Spiro-OMeTAD layers should be as thin as possible or replaced by a more transparent hole conducting material. For comparison, we also simulated a two-terminal device with a perovskite cell polarity as in the four-terminal device, i.e. where the cell is not illuminated through the Spiro-OMeTAD layer. For the constrained case with such a polarity, the pervoskite J_{sc} and the SHJ J_{sc} values reach 19.6 mA/cm^2, while the absorption in Spiro-OMeTAD is reduced to 0.5 mA/cm^2.
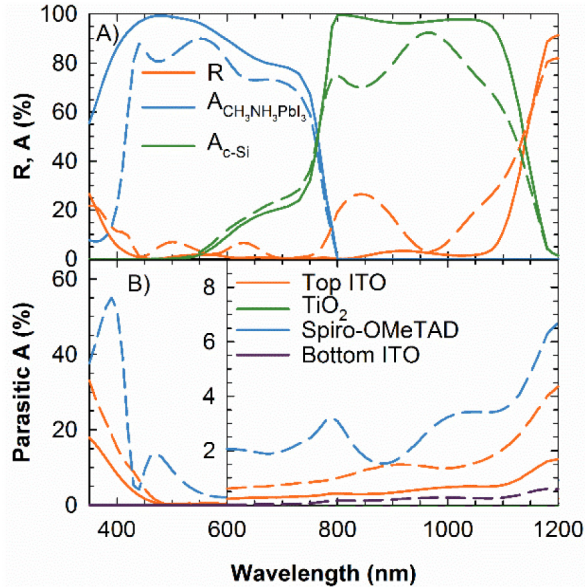
Fig. 4. Reflection and absorption plots for the flat two-terminal tandem configuration. A) Reflection of the tandem stack and absorption in the active layers. B) Parasitic absorption of layers in the $CH_3NH_3PbI_3$ perovskite cell (y-scale changes after wavelength > 600 nm). Dashed lines represent the optimal results of the constrained case, while full lines show optimum results of the unconstrained case.

To estimate how the optical behavior of the top perovskite cell changes when deposited on a random pyramid texture instead of a flat surface we simulate the incident angle dependence of the flat two-terminal cell current. The angular dependence of tandem cell J_{sc} is shown in Fig. 5. For a perovskite cell deposited on the facets of the random pyramids the incident angle of incoming light equals 54.7°. At this angle, the current for the unconstrained case drops by 5.8%, and for the constrained case by 10.2%, as compared to the normal incidence values. This J_{sc} drop can be partially recovered if the optimization is carried out at an incidence angle of 54.7°, at the expense of J_{sc} at lower angles as seen by the blue lines in Fig. 5. Therefore, we conclude that perovskite cells can be optimized for deposition on textured surfaces. To observe the effect of surface texture on reflection, we simulate a tandem with periodic pyramid texture with a characteristic angle of 54.7° using ray tracing with normally incident rays. For this we use perovskite layer thicknesses optimized for incident angle of 54.7°, since the first reflection of incident rays occurs at this angle. Second and higher-order reflections hit the pyramid surface at different angles [37]. However, as reflection is low, the second and higher-order bounces carry only a fraction of the incident power. Therefore, the optimal layer thicknesses required for the textured surface should not differ substantially from the optimum at 54.7°. The results of ray tracing simulations are shown in the last two columns in Table 5 and in Fig. 6.

The main benefit of a textured compared to a flat surface is the reduction of reflection losses, which are reduced by 3.2 mA/cm^2 and 0.5 mA/cm^2 for the constrained and unconstrained cases, respectively. This in turn results in higher J_{sc} values but also in increased parasitic absorption, since light that was reflected from a flat surface is now partially absorbed. The increase in J_{sc} due to texturing is not necessarily equal for both sub-cells, as can be seen from the J_{sc} values in the textured constrained case. This is because reflection losses for the constrained case are larger in the wavelength range where the SHJ cell absorbs light, while reflection losses in the perovskite cell absorber wavelength range are relatively

smaller. After introducing a texture, this wavelength-dependent reflection causes the SHJ current to increase more than the current of the perovskite sub-cell.
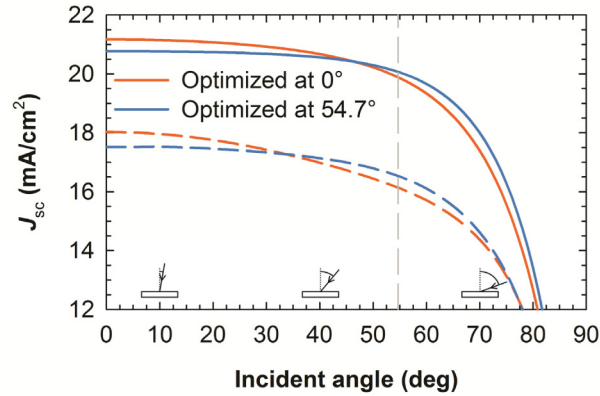

Fig. 5. Angular dependence of J_{sc} of the two-terminal tandem device. Full lines represent unconstrained thicknesses, while dashed lines show the results for constrained thicknesses. Above x-axis schematics show the incident angle.
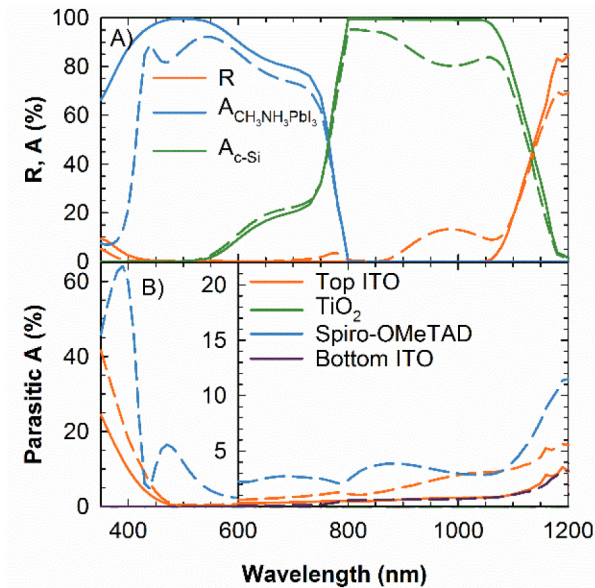

Fig. 6. Reflection and absorption plots for the textured two-terminal tandem configuration. A) Reflection of the tandem stack and absorption in the active layers. B) Parasitic absorption of layers in the CH$_3$NH$_3$PbI$_3$ perovskite cell (y-scale changes after wavelength > 600 nm). Dashed lines represent the optimal results of the constrained case, while full lines show optimum results of the unconstrained case.

For the unconstrained case, the overall reflection is already low, and using a textured surface introduces only minor current changes compared to the flat case. Owing to the optimization constraint of equal current densities at MPP and the lower fill factor of the perovskite cell, it is more beneficial to increase the J_{sc} of the perovskite than of the SHJ cell, as the unconstrained results demonstrate.

4.5 One-diode model efficiency approximations

Efficiency results for both sub-cells and the tandem cell, based on the simulated J_{sc} values and the one-diode model, are shown in Table 6. Note again that simulated values for flat front surfaces were obtained assuming a light trapping performance of a state-of-the-art SHJ cell, but without reduced reflection of the textured surface. For the four-terminal device, the efficiencies of top and bottom cell were simply added, while for the two-terminal device, the *J-V* of both cells connected in series was calculated, from which the efficiency was determined.

Table 6. Estimated efficiencies of various four-terminal (4T) and two-terminal (2T) tandem configurations based on the one-diode model and simulated J_{sc} values.

	Perovskite cell (%)	SHJ cell (%)	Tandem cell (%)
4T Constrained Flat	16.4	11.1	27.5
4T Unconstrained Flat	19.2	9.8	29.1
4T Constrained Textured	16.3	12.1	28.4
4T Unconstrained Textured	19.2	11.0	30.1
2T Constrained Flat	14.5	10.9	25.4
2T Unconstrained Flat	17.3	12.9	30.2
2T Constrained Textured	15.2	11.7	26.8
2T Unconstrained Textured	17.5	12.8	30.3

The estimated efficiency of the flat four-terminal constrained device is already higher than that of today's best single-junction SHJ cells (25.6%) [4], while the unconstrained case shows even higher efficiency, mostly due to the much better $CH_3NH_3PbI_3$ perovskite cell that has 2.8% absolute higher efficiency compared to the constrained case. The SHJ cell in the unconstrained case shows a decreased efficiency, since light up to wavelengths of 800 nm is almost completely absorbed in the perovskite cell. Introducing a textured SHJ cell raises efficiencies by 0.9% absolute and 1.0% absolute for the constrained and unconstrained case, respectively, due to reduced reflection and thus increased efficiency of the SHJ sub-cell. If a module glass with already deposited perovskite cells becomes available, this architecture can use standard SHJ or other silicon solar cells, without much adaptation.

Looking at the two-terminal device results, the flat constrained case has efficiencies comparable to the best single SHJ cells, mostly due to parasitic absorption and high reflection losses. This result indicates that it will be highly challenging to surpass the single-junction SHJ cell efficiency with flat SHJ bottom cells. On the other hand, in the flat unconstrained case, efficiencies of 30.2% are obtained, indicating that perovskite device architectures with highly transparent transport layers might still allow for highly efficient tandem devices in combination with flat SHJ cells. With a surface texture the reflection losses are even further reduced. This has the most impact on textured constrained case, where efficiencies increase by 1.4% absolute compared to the flat surface. With the unconstrained textured case the highest efficiencies of 30.3% are obtained.

The results presented above demonstrate that it is not possible to reach efficiencies above 30% with constrained thicknesses, neither with four- nor two-terminal architectures. In order to surpass 30% efficiency more transparent supporting layers are required. Spiro-OMeTAD has been identified as the most problematic and should be the first on the list for replacement with more transparent materials. ITO layers also introduce parasitic absorption losses, mostly due to free carrier absorption in near-IR. High-mobility transparent conductive oxides, giving the best compromise between resistive and free carrier absorption losses for the optimal thickness, should be used [17].

Especially for the four-terminal device increasing the absorber thickness leads to increased efficiency. An optimal four-terminal architecture requires thick perovskite layers, to absorb most light up to the absorption edge in the perovskite cell. Such structures with

absorber thicknesses up to 900 nm have already been realized (with different transport layers than Spiro-OMeTAD) and are promising candidates for tandem implementation [49]. Another possibility to increase efficiencies is to introduce a perovskite with a bandgap closer to the ideal value for a tandem with a c-Si bottom cell (1.75 eV). For the two-terminal device the absorber thickness is limited by the current matching condition. In this case, bandgap engineering of the $CH_3NH_3PbI_3$ perovskite, possible by introducing different halogens or organic groups, might be the required degree of freedom that can help to optimize devices for best possible efficiencies [22]. The polarity of the perovskite cell should be considered when new high-efficiency architectures are designed. The electron or hole transporting layer, with highest short-wavelength absorption (in our case Spiro-OMeTAD), should be positioned behind the absorber layer, so that short-wavelength light does not reach it. For the two-terminal configuration, the polarity of the SHJ cell can be easily adapted to support the series connection of the sub-cells, for example by introducing a rear emitter cell or changing the base and emitter doping type.

5. Conclusion

In this study we focused on layer thickness optimization with respect to the optical properties of tandem $CH_3NH_3PbI_3$ perovskite / SHJ cells, based on experimentally measured complex refractive index values. We compared the constrained case, where layer thicknesses were limited to experimentally accessible values, and an unconstrained case, where layers can be optically absent from the structure. The constrained cases are therefore in principle realizable with current state-of-the-art processes, while the unconstrained cases reveal the most problematic layers in terms of optical losses or insufficient absorption in the photo-active layers and show the path towards improved device architectures.

The efficiency estimates for optimized four-terminal devices exceed that of single-junction SHJ cells. Since the four-terminal device requires only minimal adaptation of the bottom SHJ cell, these devices could be readily integrated with existing industry production lines for a boost of the solar module efficiency. The challenge lies in the realization of a low parasitic absorption top cell. Integrated two-terminal devices require more complex processing, and show greater differences between constrained and unconstrained cases, but the highest efficiencies are obtained with this architecture. A textured surface of the bottom cell leads to an increase in efficiency of varying degree for all considered tandem architectures.

So far, the simulated devices were mainly inspired by their immediate experimental feasibility and ultimate devices will probably feature not only optimized thicknesses but also optimal materials and layer sequences. The benefit of our simulation approach to optical optimization is that it can be readily applied to any architecture consisting of flat layers, given that the relevant refractive index values are known.

Acknowledgments